Cancer Research

In Vivo Imaging of Tumor Metabolism and Acidosis by Combining PET and MRI-CEST pH Imaging

Dario L. Longo[1,2], Antonietta Bartoli[2,3], Lorena Consolino[2,3], Paola Bardini[2,3], Francesca Arena[2,3], Markus Schwaiger[4], and Silvio Aime[2,3]

Abstract

The vast majority of cancers exhibit increased glucose uptake and glycolysis regardless of oxygen availability. This metabolic shift leads to an enhanced production of lactic acid that decreases extracellular pH (pHe), a hallmark of the tumor microenvironment. In this way, dysregulated tumor pHe and upregulated glucose metabolism are linked tightly and their relative assessment may be useful to gain understanding of the underlying biology. Here we investigated noninvasively the *in vivo* correlation between tumor ^{18}F-FDG uptake and extracellular pH values in a murine model of HER2^{+} breast cancer. Tumor extracellular pH and perfusion were assessed by acquiring MRI-CEST (chemical exchange saturation transfer) images on a 3T scanner after intravenous administration of a pH-responsive contrast agent (iopamidol). Static PET images were recorded immediately after MRI acquisitions to quantify the extent of ^{18}F-FDG uptake. We demonstrated the occurrence of tumor pHe changes that report on acidification of the interstitial fluid caused by an accelerated glycolysis. Combined PET and MRI-CEST images reported complementary spatial information of the altered glucose metabolism. Notably, a significant inverse correlation was found between extracellular tumor pH and ^{18}F-FDG uptake, as a high ^{18}F-FDG uptake corresponds to lower extracellular pH values. These results show how merging the information from ^{18}F-FDG-uptake and extracellular pH measurements can improve characterization of the tumor microenvironment. *Cancer Res; 76(22); 6463–70. ©2016 AACR.*

Introduction

Solid tumors are characterized by a highly heterogeneous and acidic microenvironment. The combination of poor vascular perfusion, regional hypoxia, and high rates of glucose metabolism are responsible for generating extracellular acidosis in solid tumors (1). In fact, for energy production, tumor cells rely mostly on the conversion of glucose into lactate rather than mitochondrial oxidation, even in the presence of well-oxygenated conditions (Warburg effect; ref. 2). This metabolic switch toward a glycolytic phenotype occurs early in cancers, during the avascular phase, thus promoting the adaptation of the tumor cells to an acidic microenvironment. Extracellular tumor acidosis is an indicator of poor prognosis and it is known to facilitate tumor migration and invasion by the degradation of the extracellular matrix (3). Tumor acidosis has also been linked to multidrug resistance due to the neutralization of weak base chemotherapeutic drugs, which makes the drugs less efficient to cross the cellular membrane (4). It follows that the possibility of measuring precise extracellular tumor pH (pHe) at high spatiotemporal resolution is of great interest in both preclinical and clinical settings, offering selective and specific strategies for developing new treatments for solid tumors (5, 6). Moreover, the development of quantitative imaging techniques and novel imaging biomarkers is considered a key research priority in the medical imaging community (7, 8).

Currently, the gold standard for tumor detection in clinical settings is represented by [^{18}F]2-fluoro-2-deoxy-D-glucose (^{18}F-FGD) as it acts as a metabolic tracer in PET to report on the overexpression/upregulation of glucose transporters (9). ^{18}F-FDG enters the tumor cells through the GLUT 1 transporter as a glucose mimic and accumulates because it cannot be metabolized beyond the first phosphorylation step. In spite of the complexity of the ^{18}F-FDG PET methodology, ^{18}F-FDG quickly became a biomarker of outstanding importance in oncology and it is used daily in clinical settings as a surrogate marker of pathologic response and survival for a vast array of cancers (10). Despite this valuable functional information, PET imaging suffers from a limited spatial resolution that limits the information about tumor heterogeneity (11). Conversely, the superb spatial resolution of magnetic resonance imaging (MRI) allows accurate assessments of the heterogeneity of the tumor lesion. Several MRI-based approaches have been proposed for measuring tumor pH *in vivo* (12–14). Among them, the method based on chemical exchange saturation transfer (CEST) has recently gained great attention (15). This MRI approach relies on the pH-dependence of the prototropic exchange rates as measured in terms of transfer of saturated magnetization from the mobile protons to the "bulk" water resonance. As a source of mobile protons, either endogenous amide-containing molecules (16–18) or exogenous

[1]Institute of Biostructure and Bioimaging (CNR) c/o Molecular Biotechnologies Center, Torino, Italy. [2]Molecular Imaging Center, University of Torino, Torino, Italy. [3]Department of Molecular Biotechnology and Health Sciences, University of Torino, Torino, Italy. [4]Department of Nuclear Medicine, Klinikum rechts der Isar, Technische Universitat Munchen, Munich, Germany.

Note: Supplementary data for this article are available at Cancer Research Online (http://cancerres.aacrjournals.org/).

Corresponding Author: Silvio Aime, University of Torino, Via Nizza 52, Torino I-10125, Italy. Phone: 39-0116706451; Fax: 39-0116706487; E-mail: silvio.aime@unito.it

doi: 10.1158/0008-5472.CAN-16-0825

pH-responsive contrast agents (CA) can be used (19–21). Notably, within the latter class, it has been shown that the FDA-approved iodinated contrast media for X-ray computed tomography (CT) imaging can be exploited for MRI-CEST pH imaging both at preclinical and clinical levels (20, 22–25).

Currently, there is a great expectation that the combination of PET and MRI techniques in the acquisition of images of the same anatomical region may open new horizons for an improved characterization of tumor microenvironment, merging functional information delivered by PET with morphologic and functional imaging attainable by MRI. The physical integration of PET and MRI systems has already been achieved both for clinical use and for animal studies (26, 27). Therefore, by integrating MRI/PET information, the advantages of each imaging modality for assessing key features of the pathology can be exploited (28). In addition, reduction of ionizing radiation dose, in comparison to PET/CT systems, gives further support to consider PET/MRI approaches especially in longitudinal studies.

In general, one would expect that tumor extracellular pH and ^{18}F-FDG uptake are linked as the lowering of pH in the extracellular region is, first of all, the result of an increased production of glycolytic byproducts, lactate, and H^+, which are released by cancer cells to maintain physiologic intracellular pH homeostasis (29). It is therefore important to elucidate, for each tumor phenotype, whether and to what extent, ^{18}F-FDG uptake and pHe can be closely aligned biomarkers of the altered glycolytic rate. Despite the fact that aerobic glycolysis and increased extracellular acidification are recognized as hallmarks of solid tumors, no clear evidence of this relationship has been reported so far *in vivo*. In addition, it would be desirable to develop imaging approaches that can be translatable to clinical use. Here we assess the potential of MRI-CEST tumor pHe mapping at a clinical field of 3T by using the pH-responsive CA, iopamidol. We show that the combination of ^{18}F-FDG PET uptake and iopamidol-based MRI-CEST pH mapping can provide new insights for an improved characterization of tumor metabolism and microenvironment.

Materials and Methods

Materials

The following materials were used in this study: RPMI1640 medium, FBS, glutamine, penicillin, and streptomycin (Lonza Sales AG); iopamidol (Bracco Imaging Spa); ^{18}F-FDG (Advanced Acceleration Applications); phosphate-saline buffer (Sigma-Aldrich); goat serum (Sigma-Aldrich); OCT compound (Tissue Tek); primary antibody rat anti-mouse CD31 (BD Pharmigen); secondary antibody Alexa Fluor-568 goat anti-rat (Life Technologies); Hoescht33258 (Sigma Aldrich); mounting medium Fluoroshield (Sigma Aldrich). Plastic tubes containing 30 mmol/L iopamidol in PBS solutions or in tumor tissue homogenates with pH ranging from 6 to 7.4 were prepared for phantom studies. TS/A tumor tissues were homogenized with PBS at 0°C for 10 minutes in a OV5 homogenizer (Velp Scientifica). Cell fragments were separated by centrifugation at 13,000 × *g* for 20 minutes.

Tumor model

TS/A is an aggressive and poorly immunogenic murine cell line (kindly provided by Prof. Federica Cavallo, University of Torino, Torino, Italy), established from a spontaneous breast cancer from a BALB/c mouse (30). TS/A cells were maintained in RPMI1640 medium supplemented with 10% FBS, 2 mmol/L glutamine, 100 U/mL penicillin, and 100 μg/mL streptomycin and preserved in a humified incubator at 37°C with 5% CO_2. Cells were not authenticated but tested as mycoplasma-free and passaged in our laboratory for less than 6 months after their resuscitation. For the preparation of the TS/A tumor model, 2.5×10^5 cells in RPMI medium were inoculated subcutaneously into both the left and right hind limb of female 6- to 8-week-old wild-type (Charles River Laboratories) BALB/c mice, respectively. Tumors were allowed to grow for 3 to 5 weeks into tumors of suitable size that was precisely measured by MRI. To investigate the relationship between glucose uptake and tumor pHe, a first cohort of TS/A tumor bearing mice were imaged by sequential MRI and PET imaging ($n = 23$ tumors). An additional cohort of TS/A-bearing mice were split into two groups, with the first group ($n = 6$) receiving 200 mmol/L bicarbonated water *ad libitum* for 5 days to modulate tumor pHe, and the second group ($n = 6$) receiving regular drinking water. All animal procedures and husbandry were performed in accordance with the European guidelines under Directive 2010/63 and approved by the Committee on Animal Care and Use of our University.

MRI-CEST experiments

MR images were acquired on a 3T Bruker Biospec (Bruker) scanner equipped with a 30-mm quadrature RF coil. Mice were anesthetized with isoflurane vaporized with O_2. Isoflurane was used at 3.0% for induction and at 1.0% to 2.0% for maintenance. A single T_2-weighted axial slice crossing the center of the tumors was acquired with TR = 4 seconds, TE = 3.7 milliseconds, NA = 1, slice thickness = 1.5 mm, FOV = 30 × 30 mm, matrix size = 256 × 256, which yielded an in-plane resolution of 117 μm. CEST images were acquired with continuous wave (CW) RF irradiation (3 μT for 5 seconds) by using a single-shot RARE sequence (TR = 6.0 seconds, effective TE = 8.7 milliseconds, centric encoding, slice thickness = 1.5 mm, FOV = 30 mm, matrix size = 96 × 96, in-plane spatial resolution = 312 μm, NA = 1) with 46 frequency offsets unevenly distributed from −10 to 10 ppm relative to the water resonance, with the acquisition time for each *Z*-spectrum being 4 minutes 36 seconds. The CA (iopamidol) was injected intravenously into the tail vein at a dose of 4 g I/kg bodyweight.

PET imaging and analysis

A dedicated animal bed was used to shift the mice to the PET scanner immediately after the MRI acquisition (for a similar approach see ref. 31). PET static acquisitions were performed 45 minutes after the intravenous injection of ^{18}F-FDG (dose of 15 ± 3 MBq). MRI and PET/CT images were coregistered by using suitable fiducial markers on the animal bed. Mice were anesthetized with isoflurane vaporized with O_2. Isoflurane concentration was set at 3.0% for induction and at 1.0 to 2.0% for maintenance. Mice were imaged using the trimodality PET/SPECT/CT Triumph scanner (Trifoil imaging). Mice were kept fasting overnight before intravenous ^{18}F-FDG injection. PET images were followed by a CT acquisition (80 kVp, 110 mA, magnification 2.25). PET data were reconstructed using 2D-Maximum Likelihood Expectation Maximization algorithm with 10 iterations and were corrected for tracer decay and for photon attenuation. Analysis of PET images and coregistration to MR images were performed using PMOD software (http://www.pmod.com). A volume-of-interest approach was used to determine the amount of radiotracer uptake and to determine regional values for assessing the maximal percentage of the injected dose per cubic centimeter (%ID/cm^3).

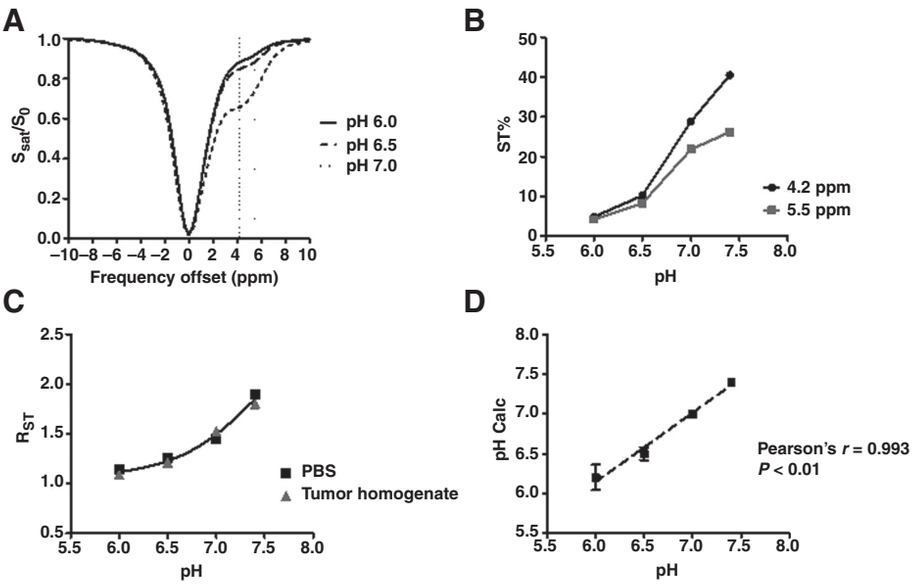

Figure 1.
Iopamidol pH responsiveness at 3T. **A,** Z-spectra of PBS-buffered solutions of iopamidol (30 mmol/L) at three representative pH values of 6, 6.5, and 7 (B_1=3 μT, RF saturation time = 5 seconds, 310K). **B,** CEST contrast (ST%) calculated from the asymmetry analysis as a function of pH. **C,** plot of the ratiometric (R_{ST}) values in the pH range from 6 to 7.4 in PBS and in tumor tissue homogenates. **D,** comparison of pH values determined by the iopamidol MRI-CEST method versus pH-meter measured values.

The SUV and SUV_{max} were obtained using the following formula: SUV = mean activity in the region of interest (MBq/g)/[injected dose (MBq)/body weight] and SUV_{max} is the maximum activity in the region of interest (MBq/g)/[injected dose (MBq)/body weight].

CEST image analysis

All data analysis was performed using custom-written scripts in Matlab (Mathworks). All Z-spectra were interpolated on a voxel-by-voxel basis, by smoothing splines, to identify the right position of the bulk water signal, by providing the B_0 inhomonogeneity correction. The interpolated Z-spectrum was shifted so that the bulk water resonance corresponds to the zero frequency and CEST contrast was quantified at a specific offset of interest (i.e., $\Delta\omega$ = +4.2/+5.5 ppm) using the asymmetry analysis:

$$ST = \frac{S_{-\Delta\omega} - S_{+\Delta\omega}}{S_0},$$

where $S_{\pm\Delta\omega}$ is the water signal intensity in the presence of the saturation pulse at offset $\pm\Delta\omega$ and S_0 is water signal intensity in the absence of the saturation pulse.

For the *in vivo* images, difference contrast maps (ΔST) were calculated by subtracting the ST contrast after iopamidol injection from the ST contrast before the injection on a per voxel basis to reduce the confounding effect of the endogenous contributions. ST maps were calculated at the frequency offsets of 4.2 and 5.5 ppm, by subtracting the corresponding precontrast ST maps. A threshold value of 2% was set, based on the ΔST variations between multiple precontrast ST maps (ca. 0.8% at 4.2 ppm and 1.7% at 5.5 μT, respectively) to discriminate between enhanced and not enhanced pixels. Ratiometric values were calculated by ratioing the difference contrast maps obtained at the frequency offsets of 4.2 and 5.5 ppm. Only those voxels showing an increase of ST contrast higher than 2%, in comparison with precontrast ST map were included for the following pH calculations. pH maps were obtained by back-calculating the pH values from the obtained ratiometric values on a voxel-by-voxel basis according to the corresponding pH calibration curve of Fig. 1C. Extravasation (perfusion) maps were assessed as the percentage of pixels showing a ΔST higher than 2% within the tumor region.

Histologic analysis

After images acquisition, mice were sacrificed and tumor tissues excised. Tumors were embedded in OCT compound and frozen in liquid nitrogen. Cryo-sections slices of 5 μm of thickness were subsequently cut and fixed in ice-cold acetone for 10 minutes and blocked with PBS containing 10% goat serum for 1 hour at room temperature. The sections were incubated with anti-mouse CD31 (1:200) overnight and then with secondary antibody (1:500) for 1 hour at room temperature. After nuclei staining with Hoescht 33258 for 10 minutes at room temperature, sections were mounted with Fluoroshield. Images were acquired with a motorised z-focus confocal microscope (Leica Microsystems).

Statistical analysis

Statistical evaluations were performed using GraphPad Prism software (GraphPad). Correlations among MRI-CEST (using pH, ΔST%, and extravasation fraction) and ^{18}F-FDG-PET (using %ID/g, SUV, and SUV_{max}) values and tumor volumes were calculated using the Pearson product-moment coefficient. Correlations were interpreted using the guidelines from Cohen (32), with absolute correlations of <0.3 considered weak, 0.3 to 0.5 moderate, and 0.5 to 1.0 strong. Statistical significance was assessed at a level of P less than 0.05.

Results

The CEST method for mapping pH using iopamidol (a widely used x-ray CA) was recently proposed and applied *in vivo* on a scanner operating at 7 T (19). As our project aims at exploring routes to transfer preclinical results to clinical applications, it was deemed of interest to work at 3T that is the magnetic field strength of the currently available PET-MRI scanners. Iopamidol MRI-CEST pH sensitivity was then first evaluated at 3T and 310K on a phantom consisting of tubes filled with aqueous PBS solutions of iopamidol

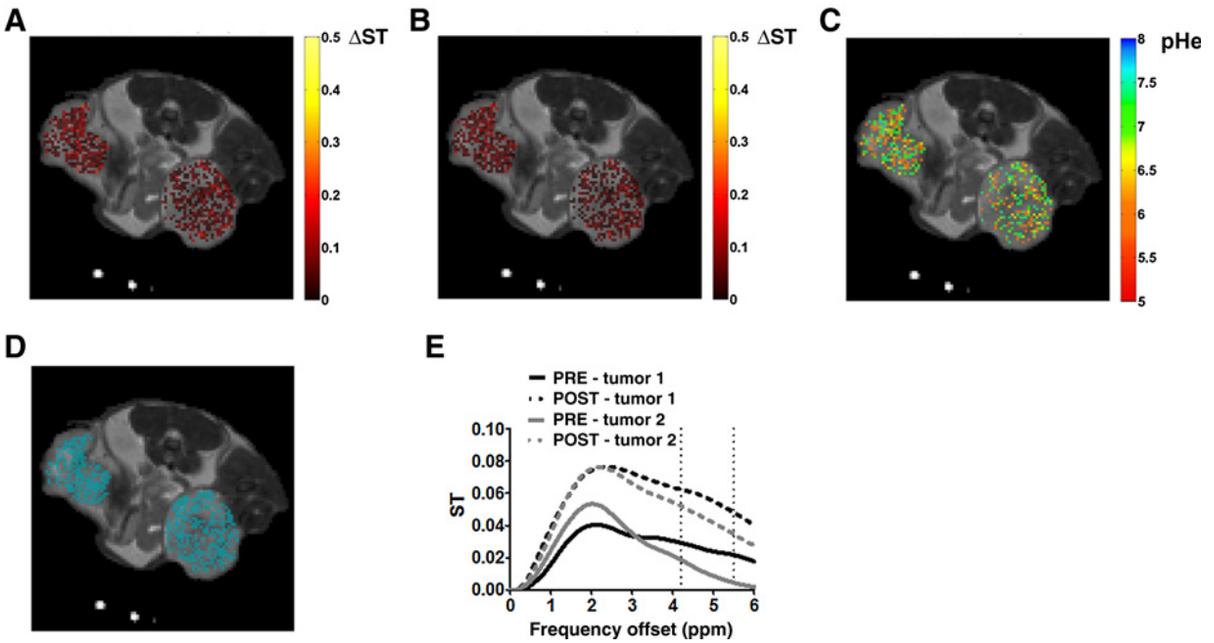

Figure 2.

Representative MRI-CEST images of a breast tumor bearing mouse showing difference ST contrast map (calculated as ΔST = ST after injection − ST before injection) at 4.2 ppm (**A**) and at 5.5 ppm (**B**), corresponding tumor pHe map (**C**), and perfusion map (**D**), showing pixels in which iopamidol has been detected (ΔST >2%), superimposed onto the anatomical T_{2w}-image. Pre- and post-iopamidol injection ST curves from ROIs including the two tumors are shown in **E**.

(30 mmol/L) at different pH, from 6.0 to 7.4. The saturation transfer (ST%) values to the bulk water signal were measured when the off-set of the irradiation fields was set at the exchanging amide proton resonances, that is, at 4.2 and 5.5 ppm, respectively. Fig. 1A shows representative Z-spectra at pH of 6, 6.5, and 7. Fig. 1B shows CEST effect (ST%) measured at 4.2 (circles) and 5.5 (squares) ppm, respectively, upon applying a saturation RF field of 3 μT for 5 seconds. ST% values steadily increase with pH for both amide proton pools. The differences in the pH dependence of ST% observed for the absorptions at 4.2 and 5.5 ppm enables the set-up of the ratiometric method for pH quantification in the physiologic range of pH from 6 to 7.4. (Fig. 1C). To assess whether the composition of the tumor tissue may affect the pH determination, the standard curve measured in PBS was compared with the one obtained in tumor tissue homogenates (Fig. 1C). Interestingly, the observed ratiometric (R_{ST}) values are very similar.

The accuracy of the pH-CEST method was evaluated by comparing the pH values calculated on the basis of the observed ST% ratios and the pH values measured by a pH meter. pH values determined from the MRI-CEST approach strongly correlates with the calibrated pH (Pearson's $r = 0.993$, $P < 0.001$), showing that a good pH accuracy is feasible at a clinical magnetic field. The pH MRI precision decreased with pH, as the SD of calculated pH was higher at lower pH, likely due to the decreased prototropic exchange rates at lower pH that results in smaller ST% effects (Fig. 1D).

MRI-CEST pHe maps were acquired *in vivo* in $HER2^+$ tumor bearing mice upon the intravenous administration of iopamidol at clinical magnetic field (3T). CEST contrast was quantified by measuring difference ST maps ($\Delta ST = ST_{post} - ST_{pre}$ iopamidol injection) to reduce confounding effects from baseline ST contrast arising from tumor endogenous components. It has been found that iopamidol is sufficiently well detected at this field, with an average ST increase from baseline values of 3% to 5% at 4.2 ppm and of 2 to 4 at 5.5 ppm, respectively (Fig. 2E). ΔST maps showed that the increase in ST contrast is highly heterogeneous in the region of interest (ROI), indicating that not all the voxels of the tumor region are vascularized, or are leaky, to a similar extent (Fig. 2A and B). As a consequence, the nonhomogeneous distribution of iopamidol is itself a read-out of the extent of perfusion in the tumor microenvironment and it directly informs about the tumor perfusion heterogeneity (Fig. 2D). Overall, about 50% to 60% of the total pixels showed an increase in ΔST values above the detection thresholds. For these pixels the corresponding tumor extracellular pH values have been computed (Fig. 2C). All the investigated $HER2^+$ breast cancer mice showed extracellular acidifications, with mean tumor extracellular pH values in the range of 6.5–7.1. Variations in pHe values within the tumors covered a range of approximately 0.6–0.8 pH units (Fig. 2C), but no marked general trend (e.g., from the core to the rim) was observed.

Validation of the proposed CEST-pH mapping approach in assessing pHe changes was performed in tumors bearing mice fed with carbonated water. The average pHe in control mice was significantly more acidic than the average pHe of tumors in mice having received 5 days of carbonated water (6.74 ± 0.07 vs. 7.01 ± 0.08, respectively; $P < 0.001$; Fig. 3A). Representative tumor pHe maps show an increase of less acidic pHe voxels in mice drinking water containing sodium bicarbonate, in comparison with control mice (Fig. 3B and C).

Figure 4 reports the results from a mouse bearing subcutaneous $HER2^+$ allograft tumors, which was sequentially imaged by a 3T MRI and a PET scanner. After the acquisition of tumor pHe map

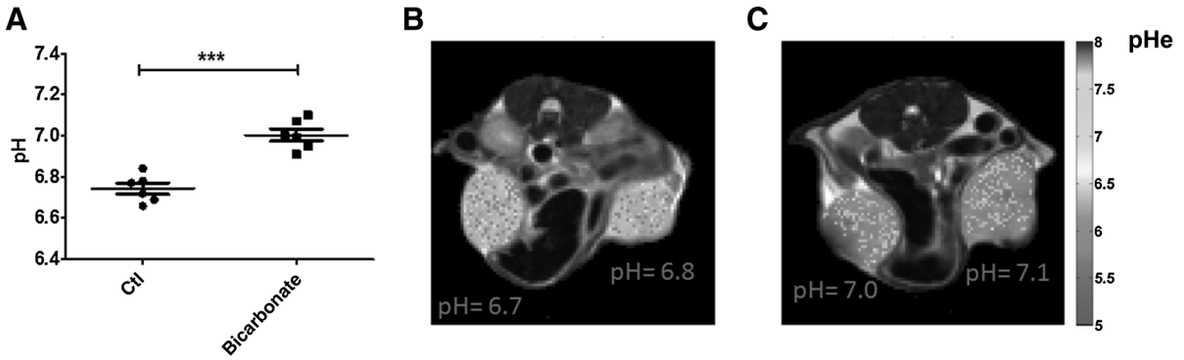

Figure 3.

A, average tumor pHe values in mice drinking natural or bicarbonated water showing a statistically significant increase of tumor pHe after 5 days of bicarbonated water. **B** and **C,** representative tumor pHe maps showing higher percentage of pixels with more acidic values for control mice (**B**) in comparison with sodium bicarbonate–treated ones (**C**).

upon iopamidol injection (Fig. 4A), static PET images show ^{18}F-FDG uptake in the tumor regions (Fig. 4B). Tumors with higher FDG uptake show lower pHe values, whereas tumors with lower FDG uptake display a less acidic microenvironment. More insight into this comparison may be gained by considering the pHe histogram analysis of the corresponding tumors (Fig. 4C). The pHe distribution values are shifted to more acidic values for the tumor characterized by an increased glucose uptake (ROI1), whereas the pHe distribution is shifted to less acidic values for the tumor with a decreased glucose uptake (ROI2). In the analyzed tumors, the ^{18}F-FDG average %ID/g ranged from 1.5% to 5.5% (mean 3.2 $\pm$ 1.1%), the SUV ranged from 0.4 and 1 (mean 0.7 $\pm$ 0.2), and the SUV_{max} ranged from 0.5 to 1.3 (mean 0.9 $\pm$ 0.3).

Finally, the relationship between the glycolytic rate and tumor acidosis was assessed between the estimates obtained from ^{18}F-FDG-PET and MRI-CEST pHe in 23 matched PET-MRI tumor images (Table 1 and Fig. 5). PET-derived parameters appear related to the tumor volume (Pearson's correlation coefficients %ID/g: $r = -0.671$, $P < 0.01$; SUV: $r = -0.710$, $P < 0.01$, SUV_{max}: $r = -0.764$, $P < 0.01$; TLG: $r = 0.467$, $P < 0.01$). A significantly strong correlation was found between ^{18}F-FDG uptake related parameters and CEST-pHe measurements (%ID/g: $r = -0.552$, $P < 0.01$; SUV: $r = -0.587$, $P < 0.01$; and SUV_{max}: $r = -0.525$, $P < 0.01$).

Insights into the heterogeneous tumor vascularization have been gained *ex vivo* by immunofluorescence staining for CD-31, which showed an extensive tumor vascular heterogeneity (Supplementary Fig. S1) analogous to that measured by CEST perfusion maps (Fig. 2D).

Discussion

To the best of our knowledge, this is the first study aimed at comparing ^{18}F-FDG uptake and extracellular pH in tumors by means of combined PET and MRI-CEST measurements. The results reported herein show that this approach is feasible and it may be a valuable tool for noninvasive imaging–based metabolic phenotyping of tumors.

^{18}F-FDG-PET imaging is a well-established, clinically used modality in the diagnosis and management of various malignancies, showing that the vast majority of cancers exhibit significantly increased glucose uptake compared with normal tissue. The increased glycolysis of tumor cells, even in the presence of adequate oxygen supplies, results in a significant decrease of the extracellular pH. There is now good evidence that the increased consumption of glucose is instrumental for the production of H^+, which promotes tumor cell migration, invasion, and angiogenesis (33). Increased

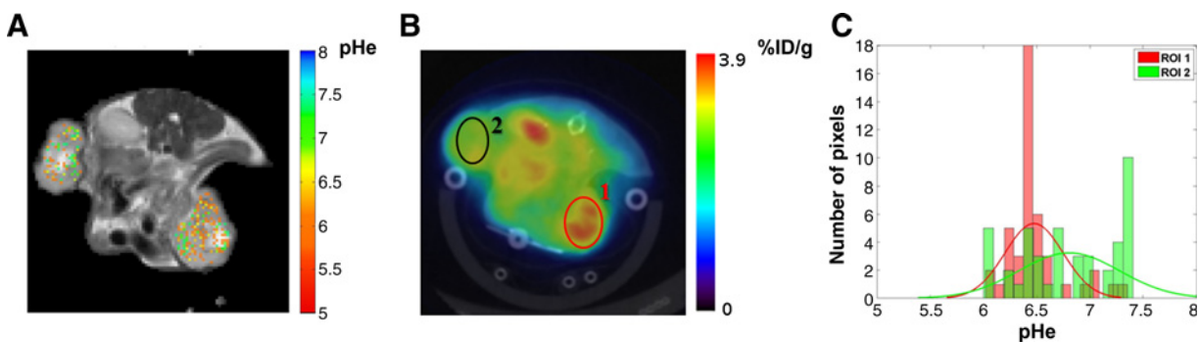

Figure 4.

Combined MRI T_{2w}/CEST pH (**A**) and PET/CT images (**B**) of a representative TS/A tumor bearing mouse with different ^{18}F-FDG uptake levels. The tumor on the right side shows a higher ^{18}F-FDG uptake in the PET image (**B**) corresponding to lower pHe values in the MRI-CEST pHe map (**A**). Distribution histogram plots of MRI-CEST pHe values (**C**) within two ROIs designed in the PET image (**B**) for tumors characterized by high (ROI 1) and low (ROI 2) ^{18}F-FDG uptake values. ROI1 shows more acidic values in comparison with ROI2 (mean pHe = 6.54 $\pm$ 0.3 and 6.8 $\pm$0.5 for ROI1 and ROI2, respectively).

Table 1. Pearson correlation coefficients for ^{18}F-FDG PET, CEST-pH data, and tumor volume

Measures	Volume	%ID/g	SUV	SUV_{max}	pH	Extravasation
Volume	1					
%ID/g	−0.671[a]	1				
SUV	−0.710[a]	0.959[a]	1			
SUV_{max}	−0.764[a]	0.932[a]	0.952[a]	1		
pH	0.519[a]	**−0.552**[a]	**−0.587**[a]	**−0.525**[a]	1	
Extravasation	0.143	0.283	0.208	0.082	−0.025	1

NOTE: All correlations were calculated using independent data points from 23 tumors. Intermodality correlations are shown in boldface type.
Abbrevations: SUV, mean standard uptake value; SUV_{max}, maximum SUV.
[a]$P < 0.01$.

glucose consumption and increased acid production are therefore tightly correlated and their relative assessment may be very useful for pursuing a better understanding of the underlying biology. The herein reported results show that a good correlation exists between ^{18}F-FDG-PET uptake (associated with the metabolic characteristics of the tumor) and MRI-CEST extracellular pH (associated with the acidification of the extracellular tumor microenvironment). In the investigated breast tumor model, we observed a significant inverse correlation between ^{18}F-FDG uptake and extracellular pH (Fig. 5). Moreover, it has been found that tumor regions with higher extracellular acidosis correspond to tumor regions with high ^{18}F-FDG uptake (Fig. 4C). Notably, the observed behavior is in agreement with the expectation that glycolysis and production of acids are increased in tumors cells compared with normal cells (34). Previous studies investigated the relationship between tumor acidosis and lactate production, but no spatial correlations have been observed, despite the large amount of lactate known to be secreted by glycolytic cancer cells (13, 35). One possible explanation is related to the role of lactate in tumor metabolism, for which recent findings have shown that is not merely the final product of glycolysis, but it can be re-used as an energetic fuel for oxidative metabolism (36). Therefore, the lack of a direct correlation between lactate and acidosis may not be unexpected due to the differential use of this molecule.

Interest in measuring and *in vivo* imaging of tumor pH has driven the development of pH-sensing CAs, in particular in the MRI field, to obtain pH maps of both extracellular and intracellular compartments (5, 14, 37). MRI-CEST based approaches have recently emerged as a powerful tool for imaging pH, thanks to the development of ratiometric methods that rule out the need to know the CA concentration (19, 23, 38, 39). In addition, our approach, in comparison with others, allow measurements of tumor pHe with high spatial resolution, high temporal resolution, and can be applied to tumors as small as few mm^3 (40). Cancers display various kinds of heterogeneity, including metabolism and vasculature, but many approaches are limited to volume-averaged tumor pHe measurements that cannot account for tumor heterogeneity (41). In contrast, CEST-pH imaging allows the noninvasive characterization of *in vivo* pHe distribution on a voxel-basis. Owing to the high spatial resolution of MRI-CEST images, the pHe values distribution within a tumor ROI can also be analyzed by conventional histogram analysis as an improved method to assess pHe heterogeneity (Fig. 4C). Our technique, owing to the injection of an extracellular agent, allows also the assessment of the extravasation fraction, a surrogate marker of tumor perfusion. We observed inhomogeneous iopamidol distribution within the tumors, likely reflecting low and high vascularized area in the heterogeneous tumor region, as confirmed by immunohistochemical analysis of

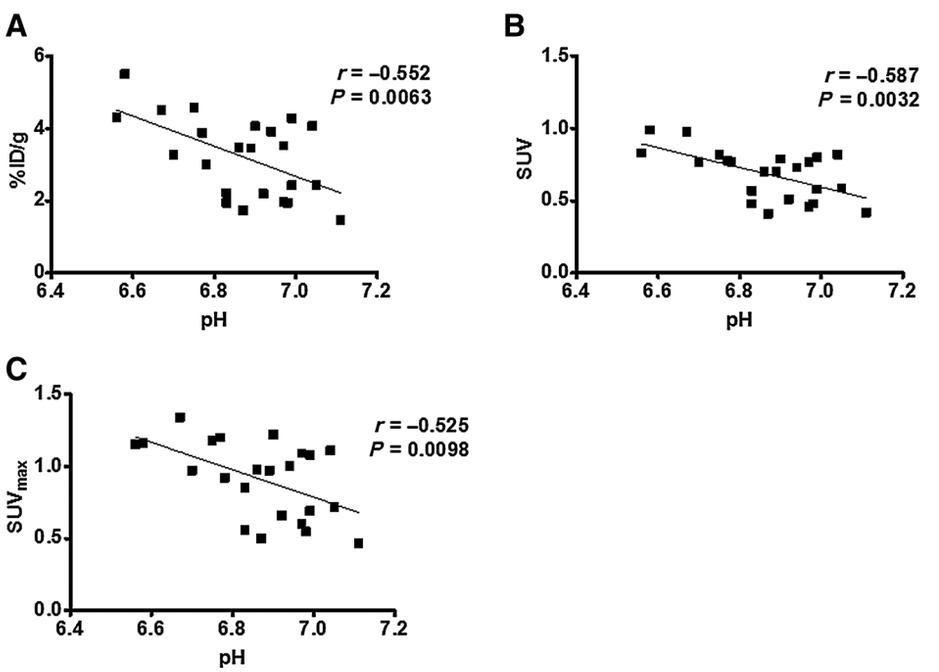

Figure 5.
Scatterplots with regression line (solid line) showing correlations between multimodality PET/MRI calculated estimates. **A,** %ID/g ^{18}F-FDG uptake as a function of extracellular tumor pH. **B,** SUV ^{18}F-FDG uptake as a function of extracellular tumor pH. **C,** SUV_{max} ^{18}F-FDG uptake as a function of extracellular tumor pH.

tumor vascularization (Supplementary Fig. S1). Similar findings have also been reported upon comparing several iodinated contrast media, in the same breast tumor model (42). It was found that the heterogeneous distribution of X-ray radiographic molecules in the extracellular–extravascular space of the tumor, as measured by the CEST approach, correlates well with the extravasation quantified by the CT approach, hence dependent on tumor vascular volume and vessel permeability characteristics. Other processes such as necrosis may also play a role in the heterogeneity, in particular for larger tumors, likely explaining the observed negative correlation between ^{18}F-FDG uptake and tumor size.

Besides the capability of measuring tumor pHe, novel proposed approaches should be able to provide a precise read-out of pH changes. It is known that administering sodium bicarbonate significantly alters tumor pHe (43). We achieved similar results with mice drinking *ad libitum* carbonated water (200 mmol/L $NaHCO_3$): the average tumor pHe in the nonmodulated mice was significantly more acidic than the average pHe of tumors in mice having received 5 days of carbonated water (Fig. 3). Therefore, our approach is sensitive enough to detect small pHe changes upon pharmacologic treatment, thus opening the possibility to exploit pH imaging as a surrogate marker of therapeutic response to novel anticancer therapies (44).

The herein reported results further strengthen the role of the MRI-CEST approaches in tumor pH-mapping. Among the several studies already available, it is worth to mention a recent report on the use of a paraCEST agent. In this work, the pH gradient in kidneys of healthy mice has been calculated by measuring the frequency of water exchange signal arising from the agent, thus introducing a further parameter for the assessment of the actual pH in addition to the ratiometric approach (45).

Overall, as the information provided by each readout (^{18}F-FDG uptake and pHe) reflects a different aspect of the same altered metabolic behavior, the combination of the two metrics should result in a synergic action of the two modalities. Furthermore, the availability of combined PET/MRI scanners for the simultaneous acquisition of molecular and functional data with high temporal and spatial fusion accuracy are already available both in preclinical and clinical environments, thus making pH mapping and ^{18}F-FDG uptake a powerful tool for tumor metabolic phenotyping (46, 47). Despite the fact that the extracellular acidity is considered a distinctive feature of cancer, the exploitation of pH sensing agents has been limited to preclinical studies, because no investigations of the methods and agents' safety profiles have been reported in patients in the proper context. On the contrary, the method presented here uses a pH-responsive agent that is a FDA-approved contrast media within the CT modality, hence a fast translation to patients for assessing tumor pHe is expected; in fact, an early phase clinical trial to estimate tumor extracellular pH in women with early-stage breast cancer is currently ongoing (48). Moreover, analogous approaches based on other (radio)-tracers specific for physiologic processes such as proliferation, hypoxia and amino acid transporters may likely widen the impact of hybrid PET/MRI measurements for tumor characterization (49, 50).

One of the limitations of our study is that pH and ^{18}F-FDG measurements have been performed on the same animal but not simultaneously on the same scanner, therefore the time gap between the two measures may likely introduce some bias on the metrics that we are comparing. However, the aim of this study was the correlation between the mean tumor values of ^{18}F-FDG uptake and pHe, and further combined MRI/PET studies will allow investigating the true temporal and spatial correlation between the two estimates.

Conclusion

In summary, the herein reported results, although limited to a breast cancer murine model, have shown the correlation between tumor extracellular pH and ^{18}F-FDG uptake. MRI-CEST tumor pH mapping provides significant, complementary information to ^{18}F-FDG-PET in the characterization of the cancer phenotype, as the high spatial resolution associated with MR images provides additional insights on tumor perfusion heterogeneity. Furthermore, as the increased acidification of the extracellular tumor microenvironment can be targeted with specific novel therapies, this combined imaging approach could be exploited as a novel imaging biomarker of therapeutic response.

Disclosure of Potential Conflict of Interest

M. Schwaiger reports receiving a commercial research grant from Siemens Medical Research; has received speakers bureau honoraria from Siemens Lunch Symposium; and has ownership interest (including patents) in Siemens. No potential conflicts of interest were disclosed by the other authors.

Authors' Contributions

Conception and design: D.L. Longo, A. Bartoli, P. Bardini, F. Arena, M. Schwaiger, S. Aime
Development of methodology: D.L. Longo, A. Bartoli, L. Consolino
Acquisition of data (provided animals, acquired and managed patients, provided facilities, etc.): D.L. Longo, A. Bartoli, L. Consolino
Analysis and interpretation of data (e.g., statistical analysis, biostatistics, computational analysis): D.L. Longo, A. Bartoli, P. Bardini, F. Arena
Writing, review, and/or revision of the manuscript: D.L. Longo, A. Bartoli, S. Aime
Study supervision: S. Aime

Grant Support

This work was financially supported by grants from the TUM-IAS (Hans Fisher Senior Fellowship; S. Aime), European Community`s Seventh Framework Programme (FP7 GLINT project 602306), and Deutsche Forschungsgemeinschaft (DFG project SFB 824).

The costs of publication of this article were defrayed in part by the payment of page charges. This article must therefore be hereby marked *advertisement* in accordance with 18 U.S.C. Section 1734 solely to indicate this fact.

Received March 18, 2016; revised August 13, 2016; accepted August 15, 2016; published OnlineFirst September 20, 2016.

References

1. Damaghi M, Wojtkowiak JW, Gillies RJ. pH sensing and regulation in cancer. Front Physiol 2013;4:370.
2. Warburg O.On the origin of cancer cells. Science 1956;123:309–14.
3. Gatenby RA, Gawlinski ET. A reaction-diffusion model of cancer invasion. Cancer Res 1996;56:5745–53.
4. Sauvant C, Nowak M, Wirth C, Schneider B, Riemann A, Gekle M, et al. Acidosis induces multi-drug resistance in rat prostate cancer cells (AT1) in vitro and in vivo by increasing the activity of the p-glycoprotein via activation of p38. Int J Cancer 2008;123:2532–42.

5. Zhang X, Lin Y, Gillies RJ. Tumor pH and its measurement. J Nucl Med 2010;51:1167–70.
6. De Milito A, Fais S. Tumor acidity, chemoresistance and proton pump inhibitors. Future Oncol 2005;1:779–86.
7. Bernsen MR, Kooiman K, Segbers M, van Leeuwen FW, de Jong M. Biomarkers in preclinical cancer imaging. Eur J Nucl Med Mol Imaging 2015;42:579–96.
8. Winfield JM, Payne GS, deSouza NM. Functional MRI and CT biomarkers in oncology. Eur J Nucl Med Mol Imaging 2015;42:562–78.
9. Shaw RJ. Glucose metabolism and cancer. Curr Opin Cell Biol 2006;18:598–608.
10. Rohren EM, Turkington TG, Coleman RE. Clinical applications of PET in oncology. Radiology 2004;231:305–32.
11. Wehrl HF, Wiehr S, Divine MR, Gatidis S, Gullberg GT, Maier FC, et al. Preclinical and translational PET/MR imaging. J Nucl Med 2014;55:11S–8S.
12. Raghunand N, Zhang S, Sherry AD, Gillies RJ. *Invivo* magnetic resonance imaging of tissue pH using a novel pH-sensitive contrast agent, GdDOTA-4AmP. Acad Radiol 2002;9:S481–3.
13. Gallagher FA, Kettunen MI, Day SE, Hu DE, Ardenkjaer-Larsen JH, Zandt R, et al. Magnetic resonance imaging of pH *invivo* using hyperpolarized 13C-labelled bicarbonate. Nature 2008;453:940–3.
14. Perez-Mayoral E, Negri V, Soler-Padros J, Cerdan S, Ballesteros P. Chemistry of paramagnetic and diamagnetic contrast agents for magnetic resonance imaging and spectroscopy pH responsive contrast agents. Eur J Radiol 2008;67:453–8.
15. van Zijl PC, Yadav NN. Chemical exchange saturation transfer (CEST): what is in a name and what isn't? Magn Reson Med 2011;65:927–48.
16. McVicar N, Li AX, Goncalves DF, Bellyou M, Meakin SO, Prado MA, et al. Quantitative tissue pH measurement during cerebral ischemia using amine and amide concentration-independent detection (AACID) with MRI. J Cereb Blood Flow Metab 2014;34:690–8.
17. Sun PZ, Sorensen AG. Imaging pH using the chemical exchange saturation transfer (CEST) MRI: Correction of concomitant RF irradiation effects to quantify CEST MRI for chemical exchange rate and pH. Magn Reson Med 2008;60:390–7.
18. Longo DL, Di Gregorio E, Abategiovanni R, Ceccon A, Assfalg M, Molinari H, et al. Chemical exchange saturation transfer (CEST): an efficient tool for detecting molecular information on proteins' behaviour. Analyst 2014;139:2687–90.
19. Longo DL, Dastru W, Digilio G, Keupp J, Langereis S, Lanzardo S, et al. Iopamidol as a responsive MRI-chemical exchange saturation transfer contrast agent for pH mapping of kidneys: *invivo* studies in mice at 7 T. Magn Reson Med 2011;65:202–11.
20. Chen LQ, Howison CM, Jeffery JJ, Robey IF, Kuo PH, Pagel MD. Evaluations of extracellular pH within *invivo* tumors using acidoCEST MRI. Magn Reson Med 2014;72:1408–17.
21. Delli Castelli D, Ferrauto G, Cutrin JC, Terreno E, Aime S. In vivo maps of extracellular pH in murine melanoma by CEST-MRI. Magn Reson Med 2014;71:326–32.
22. Longo DL, Busato A, Lanzardo S, Antico F, Aime S. Imaging the pH evolution of an acute kidney injury model by means of iopamidol, a MRI-CEST pH-responsive contrast agent. Magn Reson Med 2013;70:859–64.
23. Longo DL, Sun PZ, Consolino L, Michelotti FC, Uggeri F, Aime S. A general MRI-CEST ratiometric approach for pH imaging: demonstration of *invivo* pH mapping with iobitridol. J Am Chem Soc 2014;136:14333–6.
24. Sun PZ, Longo DL, Hu W, Xiao G, Wu R. Quantification of iopamidol multi-site chemical exchange properties for ratiometric chemical exchange saturation transfer (CEST) imaging of pH. Phys Med Biol 2014;59:4493–504.
25. Müller-Lutz A, Khalil N, Schmitt B, Jellus V, Pentang G, Oeltzschner G, et al. Pilot study of Iopamidol-based quantitative pH imaging on a clinical 3T MR scanner. MAGMA 2014;27:477–85.
26. Gaertner FC, Furst S, Schwaiger M. PET/MR: a paradigm shift. Cancer Imaging 2013;13:36–52.
27. Sauter AW, Wehrl HF, Kolb A, Judenhofer MS, Pichler BJ. Combined PET/MRI: one step further in multimodality imaging. Trends Mol Med 2010;16:508–15.
28. Haeck JC, Bol K, de Ridder CM, Brunel L, Fehrentz JA, Martinez J, et al. Imaging heterogeneity of peptide delivery and binding in solid tumors using SPECT imaging and MRI. EJNMMI Res 2016;6:3.
29. Schornack PA, Gillies RJ. Contributions of cell metabolism and H+ diffusion to the acidic pH of tumors. Neoplasia 2003;5:135–45.
30. Nanni P, de Giovanni C, Lollini PL, Nicoletti G, Prodi G. TS/A: a new metastasizing cell line from a BALB/c spontaneous mammary adenocarcinoma. Clin Exp Metastasis 1983;1:373–80.
31. Bartoli A, Esposito G, D'Angeli L, Chaabane L, Terreno E. MRI and PET compatible bed for direct co-registration in small animals. IEEE Transactions on Nuclear Science 2013;60:1596–602.
32. Cohen J.Statistical power analysis for the behavioral sciences. 2nd ed. Hillsdale, NJ: L. Erlbaum Associates; 1988.
33. Gillies RJ, Gatenby RA. Adaptive landscapes and emergent phenotypes: why do cancers have high glycolysis? J Bioenerg Biomembr 2007;39:251–7.
34. Gatenby RA, Gillies RJ. Why do cancers have high aerobic glycolysis? Nat Rev Cancer 2004;4:891–9.
35. Garcia-Martin ML, Herigault G, Remy C, Farion R, Ballesteros P, Coles JA, et al. Mapping extracellular pH in rat brain gliomas in vivo by 1H magnetic resonance spectroscopic imaging: comparison with maps of metabolites. Cancer Res 2001;61:6524–31.
36. Payen VL, Porporato PE, Baselet B, Sonveaux P. Metabolic changes associated with tumor metastasis, part 1: tumor pH, glycolysis and the pentose phosphate pathway. Cell Mol Life Sci 2016;73:1333–48.
37. Aime S, Delli Castelli D, Terreno E. Novel pH-reporter MRI contrast agents. Angew Chem Int Ed Engl 2002;41:4334–6.
38. Wu R, Longo DL, Aime S, Sun PZ. Quantitative description of radio-frequency (RF) power-based ratiometric chemical exchange saturation transfer (CEST) pH imaging. NMR Biomed 2015;28:555–65.
39. Moon BF, Jones KM, Chen LQ, Liu P, Randtke EA, Howison CM, et al. A comparison of iopromide and iopamidol, two acidoCEST MRI contrast media that measure tumor extracellular pH. Contrast Media Mol Imaging 2015;10:446–55.
40. Lutz NW, Le Fur Y, Chiche J, Pouyssegur J, Cozzone PJ. Quantitative in vivo characterization of intracellular and extracellular pH profiles in heterogeneous tumors: a novel method enabling multiparametric pH analysis. Cancer Res 2013;73:4616–28.
41. Vavere AL, Biddlecombe GB, Spees WM, Garbow JR, Wijesinghe D, Andreev OA, et al. A novel technology for the imaging of acidic prostate tumors by positron emission tomography. Cancer Res 2009;69:4510–6.
42. Longo DL, Michelotti F, Consolino L, Bardini P, Digilio G, Xiao G, et al. In vitro and in vivo assessment of nonionic iodinated radiographic molecules as chemical exchange saturation transfer magnetic resonance imaging tumor perfusion agents. Invest Radiol 2016;51:155–62.
43. Raghunand N, He X, van Sluis R, Mahoney B, Baggett B, Taylor CW, et al. Enhancement of chemotherapy by manipulation of tumour pH. Br J Cancer 1999;80:1005–11.
44. Neri D, Supuran CT. Interfering with pH regulation in tumours as a therapeutic strategy. Nat Rev Drug Discov 2011;10:767–77.
45. Wu Y, Zhang S, Soesbe TC, Yu J, Vinogradov E, Lenkinski RE, et al. pH imaging of mouse kidneys in vivo using a frequency-dependent paraCEST agent. Magn Reson Med 2016;75:2432–41.
46. Judenhofer MS, Cherry SR. Applications for preclinical PET/MRI. Semin Nucl Med 2013;43:19–29.
47. Wehrl HF, Sauter AW, Judenhofer MS, Pichler BJ. Combined PET/MR imaging–technology and applications. Technol Cancer Res Treat 2010;9:5–20.
48. University of Arizona. An early phase clinical trial to evaluate the Feasibility of CEST MRI in patients with early stage breast cancer; 2015. Available from: https://clinicaltrials.gov/ct2/show/NCT02380209.
49. Alberini JL, Boisgard R, Guillermet S, Siquier K, Jego B, Theze B, et al. Multimodal in vivo imaging of tumorigenesis and response to chemotherapy in a transgenic mouse model of mammary cancer. Mol Imaging Biol 2016;18:617–26.
50. Penet MF, Krishnamachary B, Chen Z, Jin J, Bhujwalla ZM. Molecular imaging of the tumor microenvironment for precision medicine and theranostics. Adv Cancer Res 2014;124:235–56.